Flight Dynamics of a Flying Wing Aircraft Featuring the Bell Spanload

Caleb Robb*, Rohit Vuppala*, Ryan C. Paul† and Kursat Kara†
Oklahoma State University, Stillwater, OK, 74075

Results of a previous aerodynamics study conducted over a wing that exhibits the Prandtl Bell Spanload were implemented into a simulation environment with the intent of studying unique flight characteristics that are theorized to be presented by this spanload. However, early simulations of the dynamics show that the yawing moment due to roll rate is of a higher effect than the yaw moment due to the aileron deflection angle. This over-prediction of the roll-yaw coupling term has been called into question. A new method is to be tested, which implements a compact vortex-lattice (CVLM) formulation to show the difference between the flight dynamics predicted by this new method and the stability derivative method currently in use. The analysis utilizes two initial conditions to test the differences as the dynamics propagate through time. The first, a large initial bank angle, leads to the stability derivative method diverging, while the CVLM results show this not to be the case. The second condition, a wind-field representative of a stable nocturnal boundary layer over the ground, leads to much more agreement between methods before divergence occurs due to a velocity higher than that of the stability derivative linearization point. It is then agreed that since CVLM cannot predict stall effects and other nonlinear flight regions, a hybrid approach is proposed that takes advantage of the roll-yaw coupling prediction of the CVLM and the range of conditions available to the stability derivative method.

I. Nomenclature

α	=	Angle of Attack
b	=	Span
β	=	Sideslip Angle
CFD	=	Computational Fluid Dynamics
CL	=	Lift Coefficient
CD	=	Drag Coefficient
C_l	=	Rolling Moment Coefficient
C_M	=	Pitching Moment Coefficient
C_N	=	Yawing Moment Coefficient
C_X, C_Y, C_Z	=	X-Force Coefficient, Y-Force Coefficient, Z-Force Coefficient
$c_\#$	=	Constant
dL	=	Incremental Value of L
δ_a	=	Deflection Angle for an Anti-Symmetric Aileron Deflection
δ_e	=	Deflection Angle for a Symmetric Aileron Deflection (Simulating and Elevator Deflection)
F	=	Aerodynamic Forces
g	=	Gravity
M	=	Aerodynamic Moments
m	=	Mass
ϕ	=	Roll Angle
ψ	=	Yaw Angle

*Graduate Research Assistant, Department of Mechanical and Aerospace Engineering, 201 General Academic Building, Student Member AIAA.
*Graduate Research Assistant, Department of Mechanical and Aerospace Engineering, 201 General Academic Building, Student Member AIAA.
†Assistant Professor, Department of Mechanical and Aerospace Engineering, 201 General Academic Building, Member AIAA.
†Assistant Professor, Department of Mechanical and Aerospace Engineering, 201 General Academic Building, Senior Member AIAA.

p	=	Roll Rate
q	=	Pitch Rate
r	=	Yaw Rate
θ	=	Pitch Angle
u, v, w	=	Velocity Components (Longitudinal, Lateral, Vertical)
V	=	Velocity
VLM	=	Vortex-Lattice Method
y	=	Spanwise Location

II. Introduction

THERE has been a large amount of time and effort put into studying Prandtl's Bell Spanload in the last ninety years. This solution was first developed as the minimum induced drag condition for a wing when considering a root bending-moment constraint, which stands as an analog for wing weight. Since Prandtl's Bell Spanload prediction, published in 1933, there have been many examples of predictions with different constraints, some similar to the one used by the Bell Spanload [1–3]. These analyses have shown that the root bending-moment constraint results in just one of many possible lift distributions that could be considered optimal with respect to induced drag. Every added constraint slightly modifies the lift distribution, with fairly elliptical distributions shown to be optimal in most cases if the designer is primarily considering optimizing induced drag. The use of the Bell spanload has been very sparse throughout the history of aeronautics and only recently in the research community. So, why use the Bell Spanload, as it has been shown that practical considerations, such as available fuel volume, structural weight, and Reynolds number effects, will overwhelm any potential vortex drag reductions [4]?

Perhaps the most compelling reason to consider the Bell spanload is a flight dynamics effect when traditional symmetric aileron deflections are utilized. A characteristic of a finite wing with the Bell spanload at one C_L condition is that this wing will feature an aggressive twist distribution with a large amount of washout or negative twist at the wingtip. Due to the degree of washout exhibited, a small portion of the wing near the tip experiences an interesting characteristic. Around the wingtips, there is an area where the inviscid drag induced by the wing works in the opposite direction of drag produced everywhere else on the wing. Due to the twist distribution, the resultant force on the wing is tilted slightly against the freestream in relation to the lift direction. It is important to note that this only holds true for the inviscid component of drag, with the viscous portions still working in the direction of the freestream. This, however, is still a powerful result as there is use for this effect. Since this is induced drag and is dependent on the amount of lift being generated, an increase in the lift in this section will increase the effect of the "induced thrust" [5], or a force vector that has a horizontal component opposite of the typical drag vector. A common example of this situation is when ailerons, strategically placed where the drag direction is pointing forward, are deflected. In theory, this would increase the induced drag on the deflected side in the area containing the aileron, which would work in the direction opposite of the freestream. The yaw due to aileron deflection is most often captured through the $C_{N_{\delta_a}}$ control derivative, which is expected to be positive for the Bell spanload case, opposite of a traditional aircraft. Perhaps the most compelling reason to use the Bell spanload is that, due to the region of induced thrust, an aircraft could be constructed without the vertical tail and associated drag needed to counter adverse yaw.

The research presented in this paper was motivated by attempts to study the proverse yaw phenomenon created by the Bell spanload with a positive $C_{N_{\delta_a}}$. As described in Section III, dynamics simulation cases were performed to observe the proverse yaw effect. Yet, the effect was overshadowed by roll-yaw coupling terms, most predominately C_{n_p}. To investigate the suitability of C_{N_p} prediction methods commonly used in the flight dynamics community, two plant models for the simulation are presented in this paper, and dynamic simulation results highlight different approaches to the roll-yaw coupling. The first set of analyses included the use of a vortex-lattice method [6], a computationally quick analysis tool that is widely available. Although this method is convenient, a drawback is the inviscid nature of the analysis, leading to underestimation of parameters such as drag and overestimation of the effects of certain control deflections [7, 8]. This led to the use of the second mode of analysis, a higher-fidelity computational fluid dynamics model. This analysis tool is widely used in industry and is generally known to predict results with greater accuracy than the vortex-lattice code. Our results indicate the roll-yaw coupling observed is different between the two underlying plant models.

This paper is organized as follows. Section III presents the motivation for the work, which came about using a dynamic simulation environment that uses traditional stability and control derivatives to represent aerodynamic forces. The section also presents an alternative aerodynamic model form, where the aerodynamics are evaluated at each time

step in the simulation, albeit by neglecting some of the flow physics. The paper continues with Section IV presents the high-fidelity aerodynamic model developed for the same configuration based on finite-differencing solutions of computational fluid dynamic equations at various in-flow angles. The results are readily applicable to a stability/control derivative model. Section IV.B goes on to compare the vortex-lattice solutions to the higher-fidelity solutions used later on in simulation example cases. Next, the rigid body equations of motion propagated in the simulation environment are presented in Section IV.C. The results presented in this study are for two cases, (1) is a homogeneous response of the aircraft subject to an off-trim value in the roll angle, and (2) is the trimmed aircraft response flying through a realistic wind field, developed according to the methodology in Section IV.D. Section V compares the in-the-loop aerodynamics computation to the standard stability derivative method. Interpreting the results indicates that the stability derivative approach to roll-yaw coupling is more aggressive than retaining the full inviscid aerodynamic calculations in the loop for the configuration studied.

III. Background

A flight simulation environment was initially used to test the dynamic response of the aircraft given the stability derivatives shown in Section IV. The flight simulation environment used by Dr. Andrew Arena at Oklahoma State University. The simulation allows a user to import a CAD model representation of a flight vehicle into the virtual environment and fly from a fixed vantage point on the ground or from other viewpoints with inputs from a standard RC controller or gaming joystick. A view of flying the sim from a fixed vantage point is captured in Figure 1.

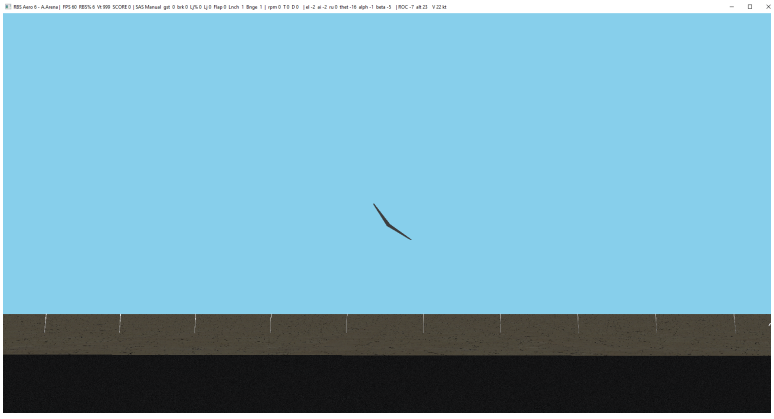

Fig. 1 Depiction of aircraft flying in the simulation environment, RBSim

Two cases were run for a flying wing shown to feature the Bell Spanload with the intent of revealing proverse yaw in one dynamic simulation and adverse yaw in the other. The change was enacted by simply changing the sign of the $C_{N_{\delta a}}$ control derivative governing adverse/proverse yaw. The cases are defined in Table 1 below:

Run Case	$C_{N_{\delta a}}$	Expectation
Case 1	Negative	Adverse Yaw
Case 2	Positive	Proverse Yaw

Table 1 Test case definitions for initial results

Following the creation of the time histories, the body-axis roll and yaw angles are plotted for Case 1 and Case 2 in Figures 2 and 3, respectively.

The Case 1 time histories match expectations. As aileron is applied, at the time stamp indicated by the dashed vertical line, the roll and yaw rate channels develop opposite signs, consistent with adverse yaw during control application. The Case 2 results are not as expected. Although the sign of $C_{N_{\delta a}}$ has been changed to positive, the roll rate and yaw rate channels again show opposite signs following the aileron application. Further investigation into the Case 2 results indicates that the roll-yaw coupling term (C_{N_p}) dominates all other factors in the Taylor series expression governing prediction of overall yaw moment, similar to Equation 12. The very low directional stability amplifies this effect in

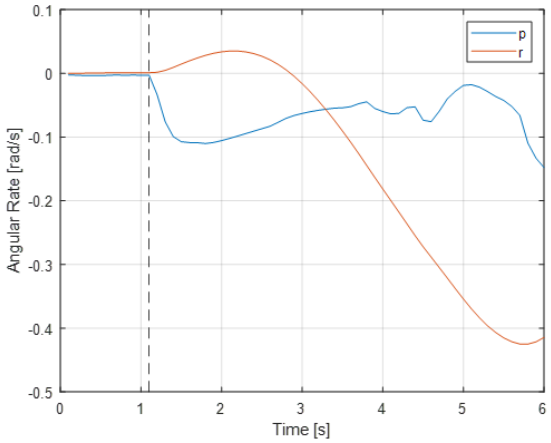

Fig. 2 Body-axis roll and yaw rate for Case 1

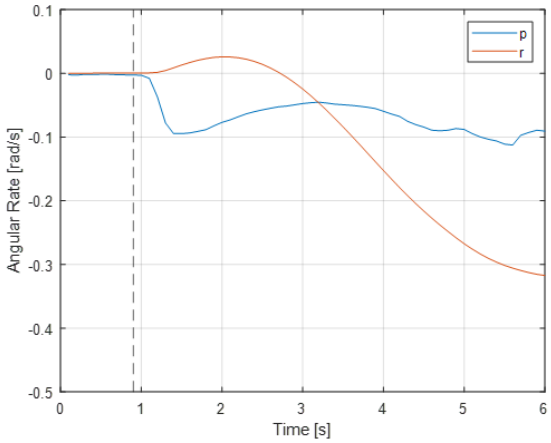

Fig. 3 Body-axis roll and yaw rate for Case 2

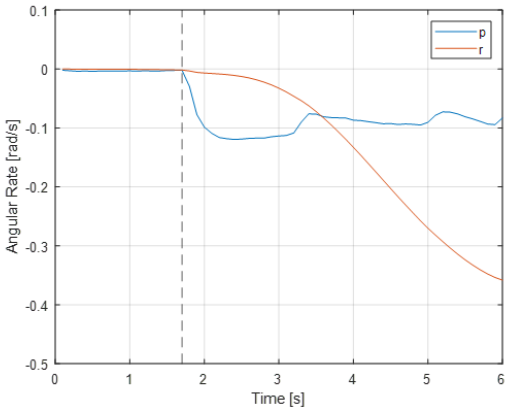

Fig. 4 Proverse yaw case - Generated by amplifying $C_{N_{\delta a}}$

the current case of a flying wing, making the dynamics highly sensitive to the value of C_{N_p} utilized. It is possible to generate state data showing proverse yaw, however an order of magnitude increase in the $C_{N_{\delta a}}$ control power compared to the results described in Section IV.B.2 was required to generate the plot in Figure 4.

A. Alternate Approach to Handling Roll Yaw Coupling

The finding from the previous section was surprising to the authors. An off-axis dynamic derivative appears to dominate the yaw moment prediction during control application for a simple flying wing configuration. Literature on roll-to-yaw coupling prediction was sparse. Most classical stability and control texts such as Refs. [9] and [10] treat the C_{N_p} term in a cursory fashion as a simple scaling of the aircraft C_L. The model in the texts would actually increase the effect of roll-yaw coupling compared to the VLM results used in this paper.

Other approaches were sought to capture the roll-yaw coupling effect. The most promising result identified so far was presented by Bunge and Kroo [11]. The reference was not directly aimed at studying aircraft dynamics. Rather, it presented what the developers deemed the Compact Vortex Lattice Method (CVLM), a formulation equivalent to a standard VLM but written in such a way that force and moment evaluation is performed via simple matrix multiplication. The computational cost of retaining all the mathematics, including the non-linearity inherent in evaluating the Kutta-Joukowski equation for force calculation via the presence of the cross-product, is zero. Rather, six matrix multiplication operations yield all six forces and moments imposed on the vehicle by the inviscid aerodynamics, with roughly the same computational cost that comes with evaluating the stability/control derivative expressions.

Much of the theoretical development of the compact VLM requires successive application of the dot-cross product

property in Equation 1.

$$(\vec{a} \times \vec{b}) \cdot \vec{c} = \vec{a} \cdot (\vec{b} \times \vec{c}) \tag{1}$$

The details of the methodology will be left to the reference. The effect on vehicle dynamics observed by Bunge and Kroo was significant and worthy of further exploration. For a sample flying wing configuration, a dynamic simulation was presented that propagated the equations of motion from a trim condition altered only by a slight angle of the bank. The aerodynamics were evaluated using (1) a stability derivative model and (2) the CVLM. In the case of the stability derivative model, the vehicle developed increasing oscillations in roll and yaw that ultimately led to the departure from controlled flight. For the case using the CVLM as the aerodynamic solver, the authors demonstrated that a limit cycle type oscillation, with a small magnitude, developed in the roll and yaw rate. No departure from a controlled flight was observed. The limit cycle must be due to the non-linearity retained in the force calculation, as limit cycle oscillations are never the outcome for linear system models.

The next step in our research is to couple the CVLM in-the-loop of a dynamic simulation environment for an aircraft with the existing flight simulation framework. Toward this goal, a version of the CVLM has been implemented in code. A flying wing test case is presented. The geometry is shown in Figures 5, where we evaluate the CVLM, and in Figure 6 from AVL as a validation tool. 50 total lattices were used in each approach, and the moments were computed about the leading edge of the wing center section.

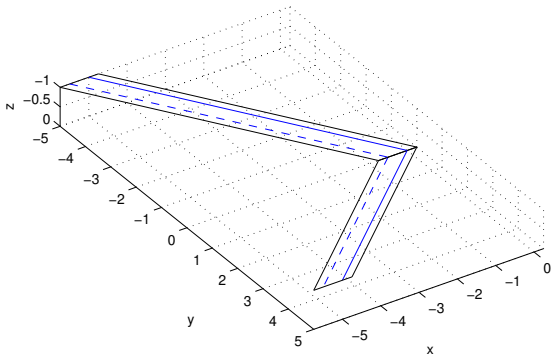

Fig. 5 Compact VLM Geometry

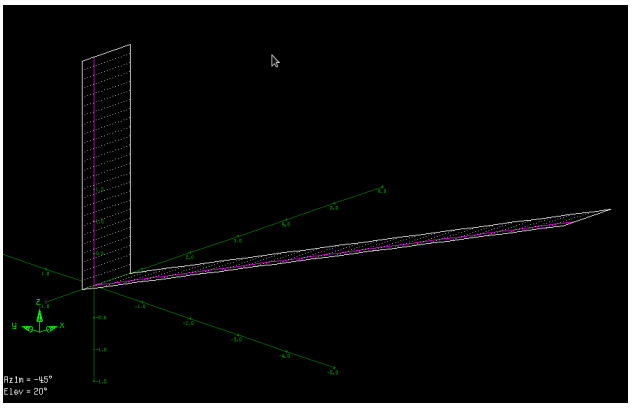

Fig. 6 AVL Geometry

Body-axis aerodynamic force and moment coefficients for the flying wing were compared to AVL at a low angle of attack (5 deg) to verify the implementation of the CVLM is correct. Table 2 shows a comparison between the two analysis methods. The table shows that the Compact VLM produces nearly the same results as AVL.

Coefficient	Our Implementation of CVLM	AVL
C_X	0.0235	0.02441
C_Y	0	0
C_Z	-0.3165	-0.31985
C_l	0	0
C_m	-0.8636	-0.87680
C_n	0	0

Table 2 Body axis force and moment coefficients for a flying wing at low angle-of-attack

IV. Methodology

To compare the two simulations, a model was created that could be run on all necessary platforms. With a plant model in place for the Bell Spanload vehicle described in Section III, this was chosen to be the model utilized. Additionally, the simulation utilized for the final results was created to simulate the effects of wind on the aircraft during flight to highlight a case where aerodynamic interactions impact the vehicle trajectory in a manner different than a homogeneous response from an off-trim initial condition. Thus, a model was generated to simulate the aircraft gliding in a wind field encountered from an initial trim condition. The process of creating this model is detailed in Section IV.D.

A. Defining the Outer Mold Line

The geometry of the aircraft tested is based on a report produced by a team from NASA Armstrong in 2016 [12]. The cross-sectional geometry was based on this paper, with the planform being a version scaled and modified as a precursor to additional research related to flight testing. The dihedral was set to be 2.5 degrees, directly pulled from the NASA report. Additionally, the taper ratio and sweep were set to 0.247 and 17 degrees, respectively. To generate the Prandtl Bell Spanload, an aggressive twist distribution was utilized. The values at each spanwise station are shown in Table 3 with Spanwise Section 0 placed at the root and 20 at the tip, with each intermediate station equally spaced across the wing.

Table 3 Twist Distribution

Spanwise Station	*Twist (degrees)*	*Spanwise Station*	*Twist (degrees)*
0	8.3274	11	7.2592
1	8.5524	12	6.6634
2	8.7259	13	5.9579
3	8.8441	14	5.1362
4	8.9030	15	4.1927
5	8.8984	16	3.1253
6	8.8257	17	1.9394
7	8.6801	18	0.6589
8	8.4565	19	-0.6417
9	8.1492	20	-1.6726
10	7.7522		

The values can then be visually represented by Figure 7 to show the heavily nonlinear nature of the distribution necessary to create this spanload.

Note that these twist values are then used as the aircraft's zero-degree angle of attack point. This varies from the traditional practice of choosing a point where the center airfoil is at zero degrees of angle of attack.

The control surface sizing and placement has taken from the report by NASA Armstrong before being scaled and modified to fit this planform. To test the validity of this placement and sizing, resources were utilized to certify these design parameters. The first is a study analyzing a similar planform to this aircraft in which the goal was to excite the proverse yaw characteristic [13]. Using this analysis as a reference, the optimal location was approximately the same as the initial design location. Using a similar reference on a more general planform [14], the placement and sizing were adequate to excite a sufficient rolling moment.

B. Developing the Aero Database

A set of both low-fidelity vortex-lattice method and higher-fidelity computational fluid dynamics results were utilized to create an aerodynamic database for a sufficient plant model. A previous study by the first author showed the difference between the results of the two solvers for this planform. This can be used to determine which parameters the vortex-lattice method solutions are adequate for and which need the higher-fidelity methods to be representative. Although the plant model is a hybrid approach, the higher-fidelity solutions were used where applicable, including all of the static components of the model.

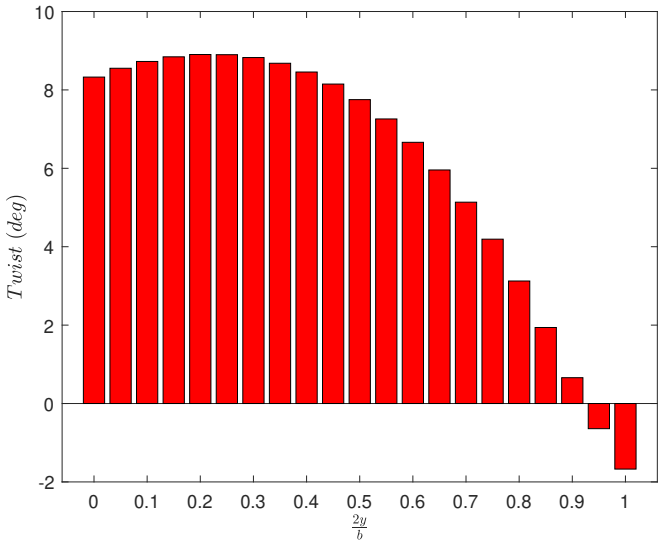

Fig. 7 Spanwise Twist Distribution

To complete the analysis, the PETE Supercomputer on the campus of Oklahoma State University was utilized. The use of this computer facilitated the CFD completed in this research, exclusively using STAR CCM+. The use of this particular software package stemmed from the first author's knowledge of the use of this software, as well as the ability to control certain parameters deemed important for the research. These parameters mainly revolve around the meshing of the wing. Throughout this process of setting up a simulation, lessons learned from the work of Dr. Seung Yoo, out of NASA Armstrong, on a similar aircraft's stall characteristics were used to tailor the mesh to increase the refinement in the areas shown to be more prone stall [15]. Additionally, a mesh refinement, again similar to one conducted by Dr. Yoo for a different aircraft [16], was conducted to ensure the results were mesh-independent. This refinement was conducted with a coarse, medium, and fine mesh.

1. Static Aerodynamic Prediction

The static aerodynamic prediction was developed directly from the CFD and validated at the design condition by comparing the lift distribution predicted by the CFD to the theoretical Bell Spanload Equation. This design condition, set to occur at a lift coefficient of 0.6, will be designed to exhibit the proverse yaw characteristic. The lift distribution at the design point can be compared to the theoretical Bell Spanload Equation in Figure 8.

With little variance shown in Figure 8, the planform can be proven to present the Bell Spanload at the design condition. This sets the groundwork for the static analysis completed in later sections.

Additionally, a drag polar can be created. This polar shows the relationship between drag and lift coefficient. This allows for visualization of the aircraft's drag properties as the lift coefficient increases.

Figure 9 shows the drag coefficient as a function of the lift coefficient around the design condition. Within a lift coefficient range of about 0.5 to 0.75, the plot is seen to be near-linear. Since the stability derivative method to be tested later relies on the linearization of aerodynamic properties for a given range of about a point, the design condition of a 0.6 lift coefficient would be a convenient point for this linearization. Additionally, post-stall effects can be simulated by linearizing a flight condition there instead of the design point. This would be advantageous for a simulation environment and is an application the CVLM is not capable of producing.

2. Stability and Control Derivative Prediction

The addition of control surfaces to the model utilized was implemented as discussed in Section IV.A. The location was placed at eighty-six percent of the half span, reaching the wingtip. This forms the entirety of the control surface

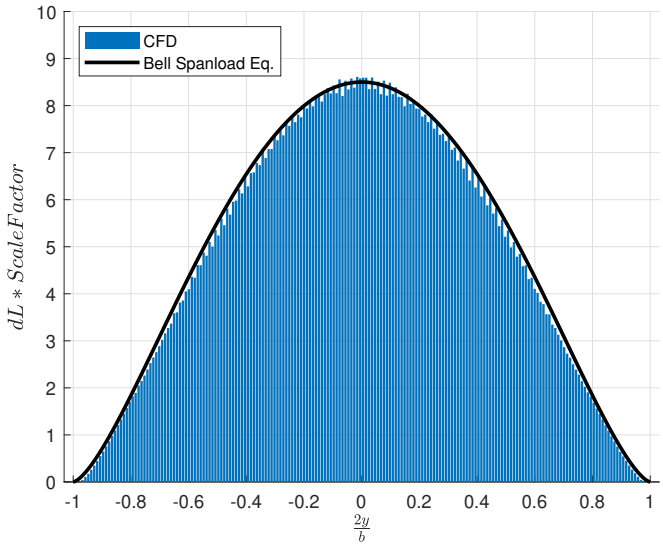

Fig. 8 Comparison Between the CFD Generated Lift Distribution and the Theoretical Bell Spanload Equation

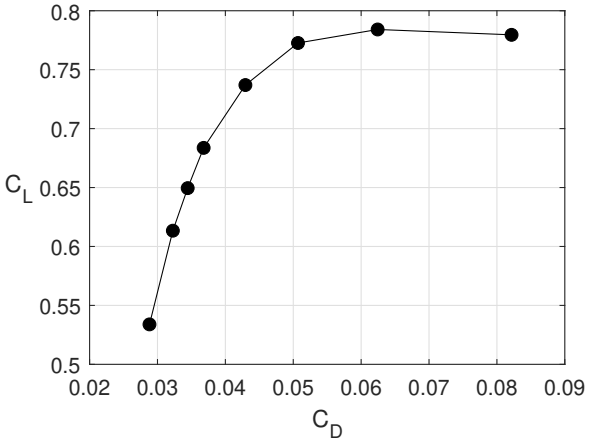

Fig. 9 Drag Polar for the Wing

effects due to the lack of more control surfaces. The control derivatives that resulted from the aerodynamic survey conducted by the first author are shown in Table 4.

Table 4 Control Derivatives

Control Derivative	*Value per Degree of Deflection*
$C_{l_{\delta_a}}$	-0.00124
$C_{N_{\delta_a}}$	-0.00000268
$C_{M_{\delta_e}}$	-0.00176
$C_{Z_{\delta_e}}$	-0.00505

The key term stemming from this analysis is the prediction of the $C_{N_{\delta_a}}$ term. This quantifies the extent of proverse yaw expected from the aircraft during a turn caused by some aileron deflection.

The stability derivatives can then be calculated by taking the slope of the plot of the parameter in question with

respect to some sideslip angle. This would occur at some point of linearization, usually trim.

Table 5 Stability Derivatives

Stability Derivative	*Value per Radian*
C_{N_β}	0.000709
C_{Y_β}	-0.002595
C_{l_β}	-0.0176

The values above were calculated using CFD results. As can be seen and must be noted going forward, the C_{N_β} is shown to be about an order of magnitude below the value recommended [17] for most aircraft. This is due to a lack of a vertical surface to help with the directional stability since this derivative characterizes a stabilizing yawing moment.

3. Dynamic Stability Derivatives

The dynamic stability derivatives were estimated from the VLM. While it is possible to apply an angular velocity to the aircraft in the CFD solver and estimate both primary and off-axis dynamic derivatives using finite differences between the force outputs with/without a rotational component in the flow field, this requires numerous additional CFD solutions and the accompanying setup and computational time. Recent flight experiments to develop aerodynamic models from system ID maneuvers have shown excellent agreement in state trajectory matching when using damping derivatives from VLM [18], giving confidence in using these values in our simulation work. The damping derivatives in our aerodynamic model are shown below in Table 7.

Table 6 Dynamic Stability Derivatives

Dynamic Derivative	*Value per Radian*
C_{Z_q}	-6.295442
C_{M_q}	-3.041993
C_{Y_p}	0.115243
C_{N_p}	-0.043580
C_{l_p}	-0.547463
C_{Y_r}	-0.002380
C_{N_r}	-0.001641
C_{l_r}	0.097951

4. Vortex-Lattice Method Comparison

Since the planform has shown that it produces the Bell Spanload at the design condition, Figure 8, the next step is the comparison between the traditional vortex-lattice method that has been used to this point and the compact vortex-lattice method (CVLM) that will be implemented into the simulation environment [19]. Figure 10 shows that the CVLM-generated results, which utilize the code QuadAir, are almost identical to the VLM outputs over the same angle of attack range and step values. They both vary from the CFD results due to the inclusion of nonlinear effects, such as stall, that are modeled in the CFD but not the other two. The response of the pitching moment coefficient to a range of angles of attack is shown in Figure 11.

Little variance can be seen between the AVL and CVLM results, with the CFD results diverging from the other two with the addition of stall effects. To show that the values generated by the QuadAir program can be utilized for the simulation, the other values related to the dynamic behavior of the system can be tested. This comparison is in the form of stability derivatives. The CVLM code was run at the design lift condition and then rotational rates were applied to the system to show the difference between the methods.

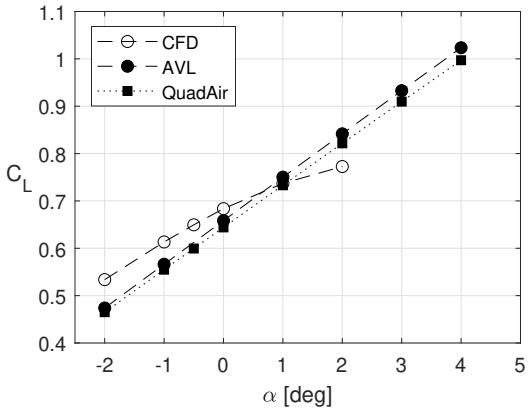

Fig. 10 Lift Curve Comparison of all Methods

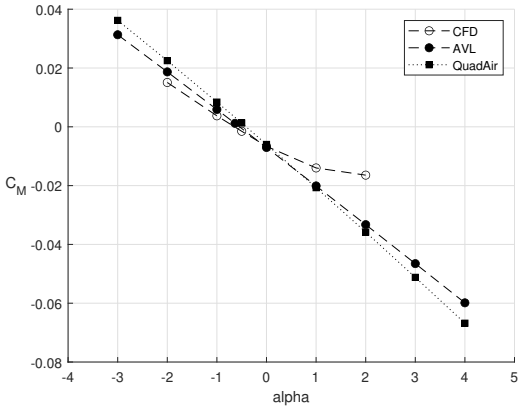

Fig. 11 Moment Coefficient Comparison of all Methods

Table 7 Dynamic Stability Derivative Comparison

Dynamic Derivative	*AVL Value*	*QuadAir Value*	*Percent Difference*
C_{Z_q}	-6.295442	-5.906	6.2%
C_{M_q}	-3.041993	-3.3646	10.6%
C_{Y_p}	0.115243	0.1288	10.7%
C_{N_p}	-0.043580	-0.03837	12.5%
C_{l_p}	-0.1547463	-0.1511844	2.3%
C_{Y_r}	-0.002380	-0.00254	6.72%
C_{N_r}	-0.001641	-0.001613	1.72%
C_{l_r}	0.097951	0.09732	0.64%

Table 7 shows the difference in the key dynamic derivatives utilized within the simulator. From this table, the maximum difference seen between any of the values is about twelve percent. It is believed that these values are acceptable for the purposes of this analysis. Additionally, a similar process can be taken to compute the control derivatives.

The results of the analysis conducted can then be implemented into the simulation environment in the form of stability derivatives. The main difference between the two methodologies is in calculating the forces and moments. The stability derivatives calculated about the linearization point are utilized to calculate the forces and moments at each time step as a simple Taylor series approximation, truncated after the first term. The results of this are then propagated

Table 8 Control Derivative Comparison

Control Derivative	*AVL Value*	*QuadAir Value*	*Percent Difference*
$C_{l_{\delta a}}$	-0.00124	-0.00134	6.35%
$C_{N_{\delta a}}$	-0.000006	-0.00000542	9.67%
$C_{M_{\delta e}}$	-0.0615	-0.0566	8.00%
$C_{Z_{\delta e}}$	-0.00387	-0.00426	10.08%

through time using the dynamics equations.

C. Incorporating the Aerodynamic Data into a Simulation Environment

The dynamic states of the vehicle are initialized to user-specified values and then propagated in real-time with the standard equations of motion for a rigid aircraft using the Runge-Kutta 4th-order method. State derivative equations in the form presented in Ref. [20] are shown below as Equations 2–11. The translational dynamics are modeled by Equations 2–4. Equations 5–7 model the rotational dynamics. Euler angles are updated via Equations 8–10 to properly project the gravitational force. The position of the aircraft in the inertial frame is updated with the expression shown as Equation 11.

$$\dot{u} = rv - qw + F_x/m - g\sin(\theta) \tag{2}$$
$$\dot{v} = pw - ru + F_y/m + g\cos(\theta)\sin(\phi) \tag{3}$$
$$\dot{w} = qu - pv + F_z/m + g\cos(\theta)\cos(\phi) \tag{4}$$

$$\dot{p} = (c_1 r + c_2 p)q + c_3 M_x + c_4 M_z \tag{5}$$
$$\dot{q} = c_5 pr - c_6(p^2 - r^2) + c_7 M_y \tag{6}$$
$$\dot{r} = (c_8 p - c_2 r)q + c_9 M_z + c_4 M_x \tag{7}$$

$$\dot{\phi} = p + \tan(\theta)(q\sin(\phi) + r\cos(\phi)) \tag{8}$$
$$\dot{\theta} = q\cos(\phi) - r\sin(\phi) \tag{9}$$
$$\dot{\psi} = (q\sin(\phi) + r\cos(\phi))/\cos(\theta) \tag{10}$$

$$\begin{bmatrix} x \\ y \\ z \end{bmatrix} = \begin{bmatrix} 1 & 0 & 0 \\ 0 & \cos(\phi) & \sin(\phi) \\ 0 & -\sin(\phi) & \cos(\phi) \end{bmatrix} \begin{bmatrix} \cos(\theta) & 0 & -\sin(\theta) \\ 0 & 1 & 0 \\ \sin(\theta) & 0 & \cos(\theta) \end{bmatrix} \begin{bmatrix} \cos(\phi) & \sin(\phi) & 0 \\ -\sin(\phi) & \cos(\phi) & 0 \\ 0 & 0 & 1 \end{bmatrix} \begin{bmatrix} u \\ v \\ w \end{bmatrix} \tag{11}$$

To propagate the translational dynamics Equations 2–4 above requires evaluation of the aerodynamic force $\begin{bmatrix} F_X & F_Y & F_Z \end{bmatrix}$ projected into the body axis. Similarly, evaluating the rotational dynamics Equations 5–7 requires knowledge of the aerodynamic moments $\begin{bmatrix} M_X & M_Y & M_Z \end{bmatrix}$ projected into the body axis. The simulation environment models the aerodynamic forces/moments by building them up in the form of traditional stability and control derivatives. An example build-up for the body-axis yaw moment coefficient is shown in Equation 12. Other forces and moment coefficients are modeled similarly to a Taylor series truncated to include only first-order terms. Non-dimensionalization of the force and moment coefficients follows standard practices.

$$C_N = C_{N_0} + C_{N_\beta}\Delta\beta + C_{N_r}\Delta r + C_{N_p}\Delta p + C_{N_\delta}\Delta\delta \tag{12}$$

In the expression, C_{N_0} is a bias term that is set to zero for symmetric configurations. C_{N_β} is evaluated at several angles of attack from the output of our static aerodynamic analysis in the CFD. The simulation takes in a user-defined

look-up table to capture variations with aerodynamic in-flow angle. The dynamic derivative terms (C_{N_r} and C_{N_p}) are evaluated in the VLM and kept constant throughout the course of the simulation. Finally, the effect of control deflection is represented by the C_{N_δ} term, which can be specified as a function of angle-of-attack by the analyst. The design of the simulation allows the user to define the stability and control derivatives using the best-available data for each contribution to the overall force/moment in each axis.

Additionally, wind effects can be added to the simulation environment in the effect of adding to the velocity components calculated at some trim conditions. This involves rotating the wind using Equation (13) to the body frame from the inertial frame.

$$R_v^b(\phi,\theta,\psi) = \begin{bmatrix} c(\theta)c(\psi) & c(\theta)s(\psi) & -s(\theta) \\ s(\phi)s(\theta)c(\psi) - c(\phi)s(\psi) & s(\phi)s(\theta)s(\psi) + c(\phi)c(\psi) & s(\phi)c(\theta) \\ c(\phi)s(\theta)c(\psi) + s(\phi)s(\psi) & c(\phi)s(\theta)s(\psi) - s(\phi)c(\psi) & c(\phi)c(\theta) \end{bmatrix} \tag{13}$$

$$V_w^b = \begin{pmatrix} u_w \\ v_w \\ w_w \end{pmatrix} = R_v^b(\phi,\theta,\psi) \begin{pmatrix} w_{n_s} \\ w_{e_s} \\ w_{d_s} \end{pmatrix} + \begin{pmatrix} u_{w_g} \\ v_{w_g} \\ w_{w_g} \end{pmatrix} \tag{14}$$

$$V_a^b = \begin{pmatrix} u_r \\ v_r \\ w_r \end{pmatrix} = \begin{pmatrix} u - u_w \\ v - v_w \\ w - w_w \end{pmatrix} \tag{15}$$

Once projected into the body frame, Equations (14)-(15) are utilized to calculate the addition of the wind to each body-axis velocity. The effect on the aerodynamic forces and moments would then be caused by this change of velocity.

D. LES Methodology for Generating Wind Data

1. Governing Equations

Cloud Model 1 (CM1) [21] was employed for the numerical simulations to generate Large Eddy Simulation data. The numerical solver works by integrating governing equations for u, v, w, π', θ', where π' is the non-dimensional pressure, θ' is the potential temperature deviations from the base state (represented by subscript "0") which is in hydrostatic balance and (u, v, w) represent the three-dimensional (3D) wind velocity field in the inertial frame. It also uses the ideal gas equation $p = \rho RT$ for determining the state variables. Dry adiabatic atmospheric conditions are considered, and the governing equations are presented below in eqs. (16) to (20):

$$\frac{\partial u}{\partial t} + c_p\theta_p\frac{\partial \pi'}{\partial x} = adv(u) + fv + T_u + N_u \tag{16}$$

$$\frac{\partial v}{\partial t} + c_p\theta_p\frac{\partial \pi'}{\partial y} = adv(v) - fu + T_v + N_v \tag{17}$$

$$\frac{\partial w}{\partial t} + c_p\theta_p\frac{\partial \pi'}{\partial z} = adv(w) + B + T_w + N_w \tag{18}$$

$$\frac{\partial \theta'}{\partial t} = adv(\theta) + T_\theta + N_\theta + \dot{Q}_\theta \tag{19}$$

$$\frac{\partial \pi'}{\partial t} = adv(\pi) - \frac{R}{c_v}\pi\left(\frac{\partial u}{\partial x} + \frac{\partial v}{\partial y} + \frac{\partial w}{\partial z}\right) + \dot{Q}_\theta \tag{20}$$

where 'adv()' represents the advection operator for a generic variable α given as $adv(\alpha) = -u\frac{\partial \alpha}{\partial x} - v\frac{\partial \alpha}{\partial y} - w\frac{\partial \alpha}{\partial z}$, where $T, \dot{Q}_\theta$ represent the tendencies from turbulence and external tendencies to internal energy (radiative cooling/heating). Furthermore, the terms N, f, and B represent the Newtonian Relaxation parameter, Coriolis parameter, and buoyancy, respectively. The turbulence tendencies in the equations could be expressed as (writing in the Einstein notations using

$(i, j = 1, 2, 3))$,

$$T_{u_{(i)}} = \frac{1}{\rho}\left[\frac{\partial \tau_{ij}}{\partial x_j}\right], \quad T_\theta = -\frac{1}{\rho}\left[\frac{\partial \tau_i^\theta}{\partial x_i}\right]. \tag{21}$$

The subgrid-stress terms are formulated as below:

$$\tau_{ij} \equiv \overline{\rho u_i' u_j'} = 2\rho K_m S_{ij}, \;\; \tau_i^\theta \equiv \overline{\rho u_i' \theta'} = -K_h \rho \frac{\partial \theta}{\partial x_i} \tag{22}$$

where S_{ij} is the strain tensor, K_m is the viscosity, K_h is the diffusivity, and K_m, K_h are determined from the type of subgrid closure used like TKE (Turbulence Kinetic Energy) similar to [22], or Smagorinsky from [23].

2. Numerical Simulation Setup

The numerical simulation was set up for a stable boundary layer, or nocturnal atmospheric boundary layer case [**?**], with the computational domain of 400 m cube. An isotropic grid resolution of 10 m is used for a coarse grid simulation. The geostrophic wind was set as 8 ms^{-1} in the East-West (x-direction) direction with a Coriolis parameter of 1.39×10^{-4} s^{-1} (73° N). Surface cooling of 0.25 K h^{-1} was employed. The potential temperature profile was initialized as a mixed layer up to 100m with a value of 265K and overlying inversion strength of 0.01 K m^{-1}. Turbulent kinetic energy (TKE) closure was employed for Sub-Grid Scale terms, and TKE was initialized as $0.4(1 - z/250)^3$ $m^2 s^{-2}$ below a height of 250 m, where z represents the height. Periodic boundary conditions on the sides, no-slip at the bottom and slip at the top, were considered. The wind data was collected after it reached a quasi-equilibrium state(8-9hr).

V. Flight Dynamics Comparison

To start the analysis, a trim condition for the aircraft was solved for an assumed airspeed. This condition was shared between both the stability derivative and compact VLM approaches for consistency in starting position. This linearization point was chosen to be convenient for the CFD results, matching the point at which these tests were run. This allows the data collected throughout the CFD testing to be used in near-trim conditions. The stability derivative method comes with the advantage of quick computational time under these conditions and ease of implementation. With a plant model available, the stability derivatives can be quickly estimated and added to the analysis.

The drawback of the stability derivative method is the prediction accuracy as the aircraft moves away from that linearization point. Ref [11] shows that the stability derivative approach leads to a divergence of results if the initial condition is far off the trim. For them, this comes in the form of some period of relatively straight flight before the aircraft starts to oscillate wildly and spin. To test the response, the aircraft was trimmed at level flight before a simulation was run with a large bank angle as an initial condition. By doing this, the aircraft was placed out of its trim condition before the dynamics were propagated.

The CVLM, on the other hand, is not dependent on the linearization point. Instead, the drawback to this method centers around the lack of usability when it comes to stall. The stability derivative method can be used during stall conditions by linearizing that area of the flight envelope. This method proves less effective when propagated through time due to the changing

A. Dynamics Comparison with an Initial Condition

For consistency between testing, a bank angle of ten degrees was chosen as the initial condition. This was the only off-trim initial condition specified to elicit a dynamic response from the simulation as opposed to steady-state translation. The CVLM analysis method is not dependent on the point at which the linearization occurred, so the item of interest is to investigate whether we see more or less roll-yaw coupling from the stability derivative method.

The trajectory in the x-y plane, Figure 12, shows that the prediction by the stability derivative method matches the CVLM for about 50 meters before diverging. The aircraft then begins to spin out of control. This also manifests as a loss of altitude, shown in the x-z trajectory plot, Figure 13, as a semi-helical shape. For the CVLM, the aircraft deviates from the zero point in the east-west direction.

Figure 14 shows the time history of the roll angle as the dynamics are propagated. The CVLM model experiences a growing oscillation before a relatively constant amplitude of about 20 degrees is reached for multiple consecutive

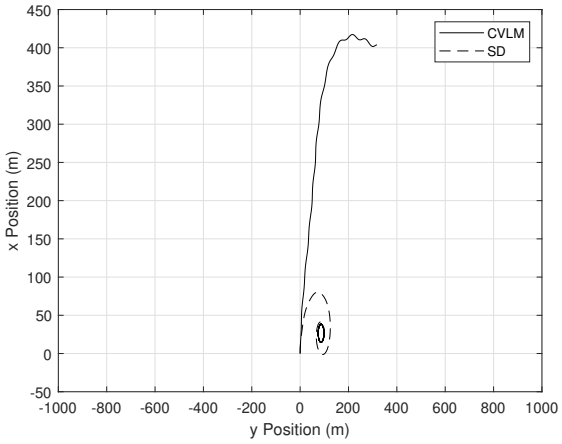

Fig. 12 X-Y Trajectory Plot Comparison

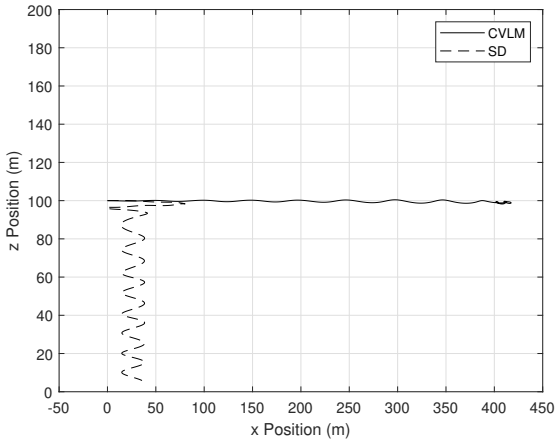

Fig. 13 X-Z Trajectory Plot Comparison

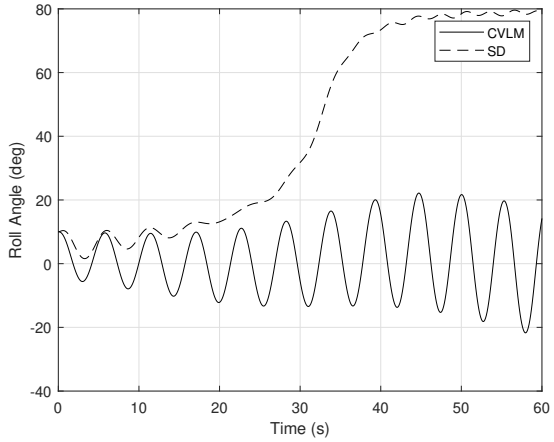

Fig. 14 Roll Angle Time History

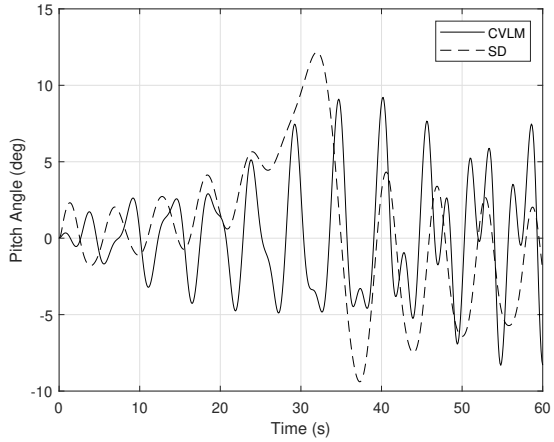

Fig. 15 Pitch Angle Time History

oscillations. The stability derivative method shows less oscillation behavior initially before diverging to a large roll angle just before 30 seconds. This is accompanied by a spike in the pitch angle, shown in Figure 15. The pitch angle is shown to oscillate rapidly with non-uniform behavior and amplitude.

The roll rate of both models, Figure 16, presents an interesting comparison. The CVLM results show slightly more oscillations whose amplitudes are higher in magnitude than the stability derivative. This can be explained by the lack of correction the stability derivative method shows after the initial angle. There is some correction before the damping term causes the aircraft to oscillate in an off-term condition, causing the divergence in results. The yaw rate plot, shown in Figure 17, shows a large divergence through time as the aircraft starts to spiral. Conversely, the CVLM results show more stability with more regular oscillations.

As was stated in Section III, the C_{N_p} term was determined to be the term the stability derivative model was most sensitive to. This term could be seen to overshadow the $C_{N_{\delta a}}$ term, negating any proverse yaw that could be expected from the aircraft.

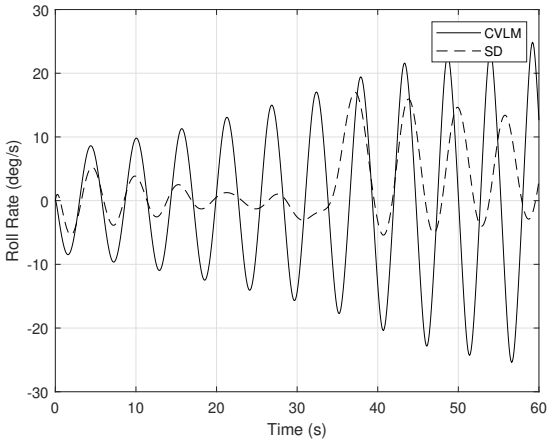

Fig. 16 Roll Rate Time History

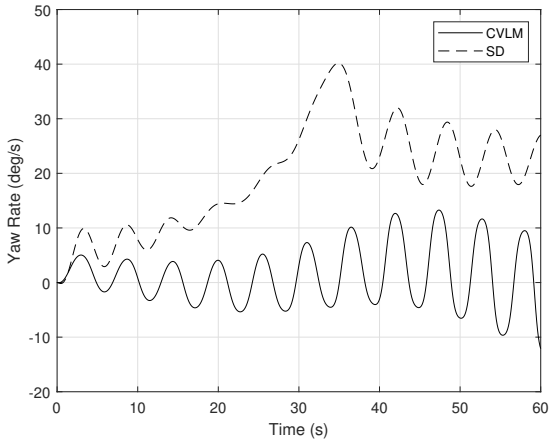

Fig. 17 Yaw Rate Time History

B. Dynamics Comparison Through a Wind-Field

To further test the difference in dynamics predicted by these two methods, a wind field was generated through the methodology presented in Section IV.D. For simplicity of implementation, a nocturnal atmospheric boundary layer case was utilized with an initial altitude that would prove to be a major contributor to the dynamics. The variation of the wind speed with altitude can be visualized at a time step in both the north and east directions with a contour plot of the results.

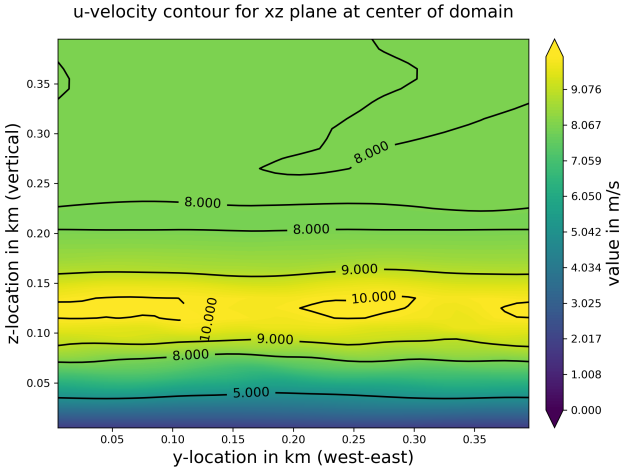

Fig. 18 u component (x-direction) of velocity in the xz plane at the center of the domain

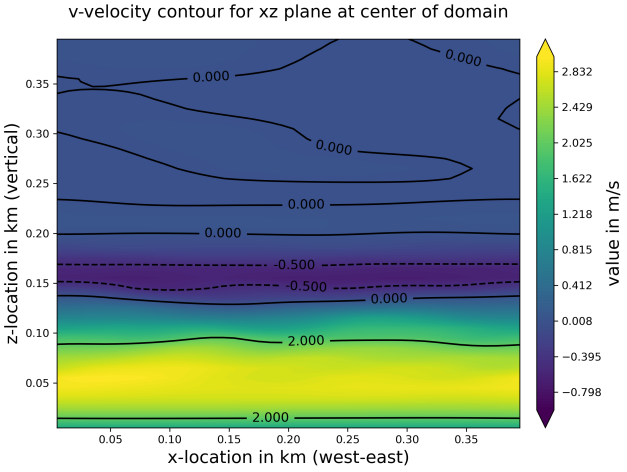

Fig. 19 v component (y-direction) of velocity in the xz plane at the center of the domain

Where the wind speed reported on the bar is in m/s. This shows a relatively large side wind at the lower altitudes on the graph with a high x-direction velocity across the rest of the field.

Both models were then run through this wind field without the initial bank angle to compare the two simulations. The initial condition that most drives the results of this simulation is the altitude. As can be seen, by Figure 19, the east-west blowing wind will introduce a non-trim condition in the form of some velocity in the y-direction, v. For this set of analyses, the altitude was chosen to be 100m above ground level. This altitude allows for some y-direction wind to affect the aircraft while also exploring the effects of the highest x-direction wind.

The trajectories plotted in Figures 20 and 21 show a much longer period of agreement before variation occurs.

The deviation from the trim condition seems to come in the form of rates. There is an agreement between the two methods on the extent of these rates before eventually deviating enough from the design condition that the results diverge. Large roll rates are predicted from both models, with the stability derivative model predicting more stable behavior.

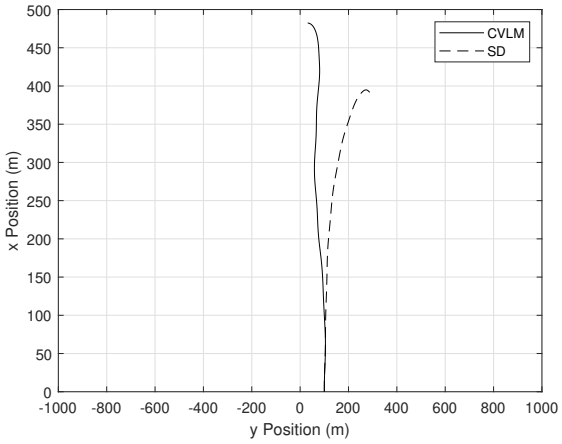

Fig. 20 X-Y Trajectory Plot Comparison

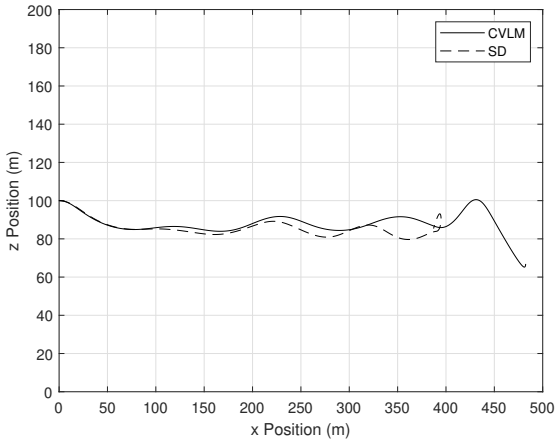

Fig. 21 X-Z Trajectory Plot Comparison

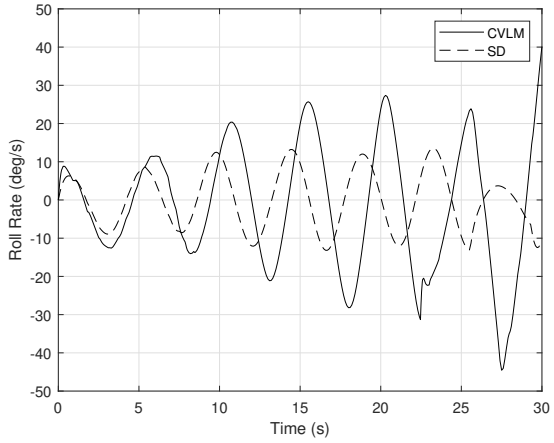

Fig. 22 Roll Rate Time History

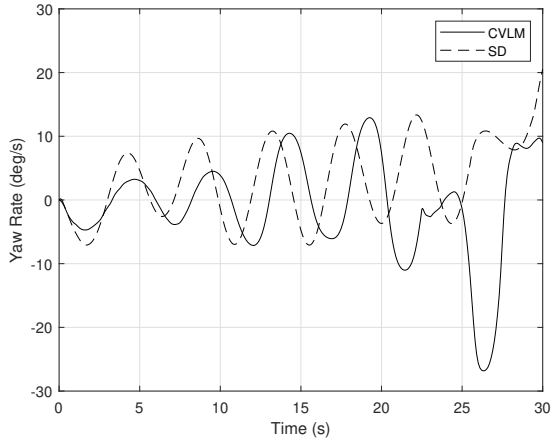

Fig. 23 Yaw Rate Time History

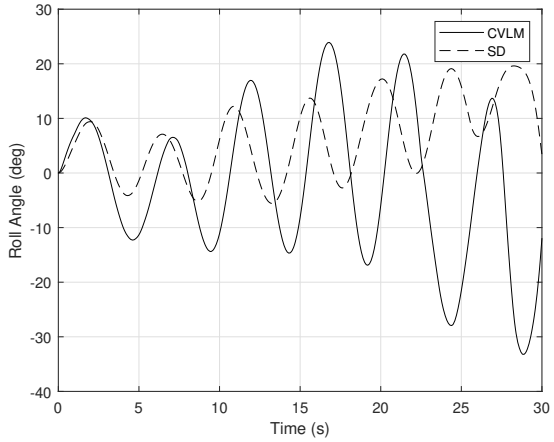

Fig. 24 Roll Angle Time History

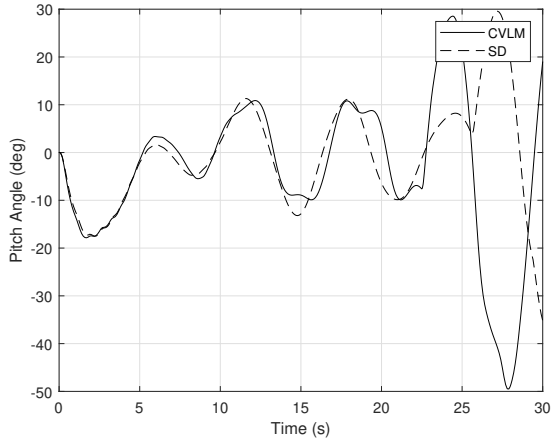

Fig. 25 Pitch Angle Time History

The roll angle follows the same trend in Figure 24. An initial increase is seen before the plot begins to oscillate. The CVLM results show increasing oscillations in the negative roll angle direction while the stability derivative shows smaller amplitude oscillations that trail in the positive roll angle direction. The pitch angle shows similar behavior in Figure 25. A large initial pitch down for both models is predicted with growing, erratic oscillations shown.

VI. Conclusions

This paper applies aerodynamic modeling techniques to an aircraft that features the Prandtl Bell Spanload in an attempt to recreate the proverse yaw concept indicated by the sign of $C_{N_{\delta a}}$. While this was shown to initially produce a small amount of proverse yaw in a dynamic simulation, another term, C_{N_p}, overshadows its effects on the dynamics, negating any of the effects of the $C_{N_{\delta a}}$ term. This huge dependency on a couple of terms was initially a surprise, leading to the analysis conducted in this paper. With a CVLM implementation, the aerodynamic forces and moments can be quickly calculated at any time step.

This analysis led to the implementation of two methodologies related to the prediction of the dynamics of the aircraft with two different initial conditions. The first test was an initial bank angle. This presented as a condition of the range linearized in the analysis, leading to the results eventually diverging, particularly in the roll and yaw axis. This presents an example of a situation in which the stability derivative model would break down, given the large initial offset from the linearization point. Since the CVLM does not depend on a specific point of linearization, the same effect is not seen for these results. This did, however, show that the roll-yaw coupling that can be seen to plague the stability derivative method is not as present within the CVLM, with much less divergent behavior predicted.

The second condition tested was through a generated wind field presenting heavy eastward wind. This was an expansion related to testing of the differences between the two methods. Since the initial condition was left without a bank angle, the initial behavior, near the trim condition, matches the models very well. The aircraft then starts to become unstable due to the lack of pilot input to control the aircraft in the higher airspeed and much higher y-direction velocity. Since this becomes an off-trim point, the aircraft can be seen to oscillate within both sets of results. However, the stability derivative method does not seem to diverge to the same extent as the previous condition.

Future work related to this project would be the utilization of both methodologies in a simulation environment similar to that discussed in Section III. The CVLM could be implemented to calculate the coupling effects at each time step while the traditional stability derivative approach would be used for the other terms to retain the ability to model nonlinear areas of the flight envelope, particularly stall. Since the plant model can be linearized over any range of flight conditions, with user discretion due to errors related to the size of this range, there is more broad applicability to this method. A hybrid approach would allow further testing related to this coupling effect as the CVLM would model the coupling terms while the stability derivative approach could be used to take advantage of the ability to linearize nonlinear regions of the plant model. This can then be used to estimate the aerodynamic forces and moments at each time step to create a cohesive flight simulation.

Acknowledgments

The authors are grateful to Dr. Aaron Alexander for his guidance in performing the computational fluid dynamics simulations in this paper, and to Dr. Andrew Arena for the use of his simulation environment. Additionally, Dr. Roberto Bunge's support in answering some questions about his CVLM technique is appreciated.

Financial support for the first and third authors was provided by the National Aeronautics and Space Administration under a sub-award of Grant 80NSSC19M0058 issued through the Oklahoma NASA EPSCoR Program. Their support is gratefully acknowledged.

Financial support for the second and fourth authors was provided by the National Science Foundation under Grant No. 1925147.

The computing for this project was performed at the High-Performance Computing Center at Oklahoma State University supported in part through the National Science Foundation grant OAC-1531128.

References

[1] Phillips, W. F., Hunsaker, D. F., and Taylor, J. D., "Minimising induced drag with weight distribution, lift distribution, wingspan, and wing-structure weight," *The Aeronautical Journal*, Vol. 124, No. 1278, 2020, pp. 1208–1235.

[2] Phillips, W., Hunsaker, D., and Joo, J., "Minimizing induced drag with lift distribution and wingspan," *Journal of Aircraft*, Vol. 56, No. 2, 2019, pp. 431–441.

[3] Pate, D. J., and German, B. J., "Lift distributions for minimum induced drag with generalized bending moment constraints," *Journal of Aircraft*, Vol. 50, No. 3, 2013, pp. 936–946.

[4] Kelly, C., "The Application of Ludwig Prandtl's Bell-Curve Span Loading to a Straight, High Performance Sailplane Wing," Master's thesis, Oklahoma State University, 2021.

[5] Bowers, A. H., "On the Minimum Induced Drag of Wings," *Slides of the conference presented at the Soaring Valley Soaring Club, January 21st*, 2006.

[6] Drela, Mark and Youngren, Harold, "Athena Vortex Lattice," , 2010. URL `http://web.mit.edu/drela/Public/web/avl/avl_doc.txt`.

[7] Cummings, R. M., Mason, W. H., Morton, S. A., and McDaniel, D. R., *Applied computational aerodynamics: A modern engineering approach*, Vol. 53, Cambridge University Press, 2015.

[8] Park, S., "Modeling with vortex lattice method and frequency sweep flight test for a fixed-wing UAV," *Control Engineering Practice*, Vol. 21, No. 12, 2013, pp. 1767–1775.

[9] Etkin, B., and Reid, L. D., *Dynamics of flight*, Vol. 2, Wiley New York, 1959.

[10] Nelson, R. C., et al., *Flight stability and automatic control*, Vol. 2, WCB/McGraw Hill New York, 1998.

[11] Bunge, R., and Kroo, I., "Compact formulation of nonlinear inviscid aerodynamics for fixed-wing aircraft," *30th AIAA Applied Aerodynamics Conference*, 2012, p. 2771.

[12] Bowers, A. H., Murillo, O. J., Jensen, R. R., Eslinger, B., and Gelzer, C., "On wings of the minimum induced drag: Spanload implications for aircraft and birds," Tech. rep., 2016.

[13] Hainline, K., Richter, J., and Agarwal, R. K., "Vehicle Design Study of a Straight Flying-Wing with Bell Shaped Spanload," *AIAA Scitech 2020 Forum*, 2020, p. 0007.

[14] Brincklow, J. R., Montgomery, Z. S., and Hunsaker, D. F., "Controlling Roll-Yaw Coupling with Aileron Placement and Wing Twist," *AIAA Scitech 2021 Forum*, 2021, p. 0327.

[15] Yoo, S., "Computational Fluid Dynamics Analysis of the Stall Characteristics of a Wing Designed Based on Prandtl's Minimum Induced Drag," *2018 Applied Aerodynamics Conference*, 2018, p. 3009.

[16] Yoo, S., and Duensing, J., "Computational Analysis of the External Aerodynamics of the Unpowered X-57 Mod-III Aircraft," *AIAA Aviation 2019 Forum*, 2019, p. 3698.

[17] Raymer, D., *Aircraft design: a conceptual approach*, American Institute of Aeronautics and Astronautics, Inc., 2012.

[18] Simmons, B. M., McClelland, H. G., and Woolsey, C. A., "Nonlinear model identification methodology for small, fixed-wing, unmanned aircraft," *Journal of Aircraft*, Vol. 56, No. 3, 2019, pp. 1056–1067.

[19] Bunge, R., "QuadAir," `https://github.com/rbunge/QuadAir`, 2014.

[20] Morelli, E. A., and Klein, V., *Aircraft system identification: theory and practice*, Vol. 2, Sunflyte Enterprises Williamsburg, VA, 2016.

[21] Bryan, G. H., and Fritsch, J. M., "A benchmark simulation for moist nonhydrostatic numerical models," *Monthly Weather Review*, Vol. 130, No. 12, 2002, pp. 2917–2928.

[22] Deardorff, J. W., "Stratocumulus-capped mixed layers derived from a three-dimensional model," *Boundary-Layer Meteorology*, Vol. 18, No. 4, 1980, pp. 495–527.

[23] Smagorinsky, J., "General circulation experiments with the primitive equations: I. The basic experiment," *Monthly weather review*, Vol. 91, No. 3, 1963, pp. 99–164.